A THIRD-ORDER MULTIRATE RUNGE–KUTTA
SCHEME
FOR FINITE VOLUME SOLUTION
OF 3D TIME-DEPENDENT MAXWELL'S
EQUATIONS

MARINA KOTOVSHCHIKOVA,
DMITRY K. FIRSOV AND SHIU HONG LUI

msp

msp

A THIRD-ORDER MULTIRATE RUNGE–KUTTA SCHEME
FOR FINITE VOLUME SOLUTION
OF 3D TIME-DEPENDENT MAXWELL'S EQUATIONS

Marina Kotovshchikova, Dmitry K. Firsov and Shiu Hong Lui

A third-order multirate time-stepping based on an SSP Runge–Kutta method is applied to solve the three-dimensional Maxwell's equations on unstructured tetrahedral meshes. This allows for an evolution of the solution on fine and coarse meshes with time steps satisfying a local stability condition to improve the computational efficiency of numerical simulations. Two multirate strategies with flexible time-step ratios are compared for accuracy and efficiency. Numerical experiments with a third-order finite volume discretization are presented to validate the theory. Our results of electromagnetic simulations demonstrate that 1D analysis is also valid for linear conservation laws in 3D. In one of the methods, significant speedup in 3D simulations is achieved without sacrificing third-order accuracy.

1. Introduction

Many real life simulations require complicated geometries and highly nonuniform meshes. When explicit methods are used, the maximum allowed time step is defined by the smallest elements in the mesh. When a fine mesh is required only in a small region of a computational domain, it is not a desirable expense. In addition, when a small time step is used on a coarse grid, it often generates dissipation in the solution. To overcome the need for a restrictive time step, local time-stepping (LTS) or multirate methods are very useful. In this case local stability conditions (CFL) are imposed on subdomains of the computational domain in place of a global more restrictive stability condition.

The earliest works on multirate methods include multirate Runge–Kutta schemes by Rice [32] and Andrus [2; 3], multirate linear multistep by Gear and Wells [16], and local time-stepping with forward Euler by Osher and Sanders [30]. Over the last three decades multirate versions of many traditional temporal schemes, such as explicit Runge–Kutta [10; 11; 20; 27; 38], Adams–Bashforth [33], as well as implicit-explicit (IMEX) methods [34] were designed.

In the computational electromagnetics literature one can find LTS versions of leap-frog schemes [9; 29; 18; 4], multistage (Runge–Kutta, predictor-corrector) [4; 15] and multistep (Adams–Bashforth) explicit methods [17; 19], Cauchy–Kovalevskaja procedures [39], and locally implicit time integration [12]. In [8] a method based on Yee's scheme with special discrete transmission conditions for unknown values at the interface between LTS subdomains was developed, and applied to the 3D Maxwell's equations in [9]. A space-time mesh refinement method is implemented with a discontinuous Galerkin (DG) space discretization for first-order hyperbolic systems in [14]. The advantage of the space-time mesh refinement method is that it guarantees the stability of the scheme by enforcing conservation of discrete energy. But it requires solution of a linear system at the interface between two grids at each time step. This becomes more and more computationally expensive as we increase the number of multirate domains in 3D space. An LTS method based on the symplectic Störmer–Verlet scheme was proposed by Piperno in [31]. The scheme with two levels of refinement was proven to conserve discrete energy. In [29] Montseny et al. followed the same idea to develop a leap-frog-based LTS scheme. In both cases time increments proportional to 2 are used and the latest available solution is used for coupling at the interface between domains with different time steps. In [13] Diaz and Grote derived an arbitrary (even) high-order LTS method for the second-order wave equation. Their method is based on an extension of the second-order leap-frog scheme by a modified equation approach [36]. The method was proven to conserve discrete energy under some CFL condition. Its implementation for the 2D Maxwell's equations can be found in [18]. An LTS method based on Adams–Bashforth multistep schemes was developed by the same authors in [19], and another implementation can be found in [17]. In [39] an LTS technique based on the arbitrary high-order derivatives (ADER) DG method was proposed. Unlike methods based on multistage time integration, there is no consistency challenge between solutions at different time increments in the ADER approach. This allows for a more flexible distribution of local time steps with optimal performance. A causal-path LTS technique utilizing multistage time schemes has been proposed by Angulo et al. in [4]. It was applied to Maxwell's equations using fourth-order RK and second-order leap-frog as base time integration schemes. Their LTS approach requires a computation of the stage value of neighbors in order to advance the solution on a given subdomain. Therefore, the idea is similar to the one proposed by Tang and Warnecke in [38].

In this work we analyze and implement two LTS approaches based on third-order strong stability preserving (SSP) Runge–Kutta to improve efficiency of third-order-accurate 3D electromagnetic simulations. One is a third-order extension of the idea proposed by Tang and Warnecke [38]. It is based on a projection of the solution to provide consistent coupling at LTS interfaces. Another one uses interpolation

of stage values for the same purpose [27]. Both schemes allow arbitrary time-step ratios and are relatively inexpensive to implement with any 3D finite volume scheme on tetrahedral meshes. The flexible time-step ratio gives more optimal simulation speedup on nonuniform meshes with large differences in cell size without loss of accuracy. A linear version of order conditions is used to analyze the accuracy of both schemes. Our analysis shows that a third-order extension of the scheme from [38] leads to only a first-order coupling, while the scheme proposed in [27] maintains third-order accuracy. Both schemes are implemented for the 3D time-domain Maxwell's equations with a third-order finite volume spatial approximation. Two strategies to define local time-step distribution are compared. One is a traditional power of 2 base partition, and another one is based on a more flexible time-step ratios and optimization algorithm. Numerical results in 1D and 3D with both schemes confirm our theoretical results. Moreover, both proposed time-step distribution strategies lead to the same accuracy in our simulations confirming flexibility of considered schemes. Significant speedup is observed in both schemes for problems with large linear cell-size ratio.

The paper is organized as follows. Section 2 describes Maxwell's equations in the time domain and their finite volume discretization. Section 3 discusses multirate Runge–Kutta schemes in 1D and their accuracy analysis for linear problems. In Section 4 a 3D implementation of algorithms using arbitrary time-step distribution is presented. Finally, Section 5 shows numerical validation of third-order LTS schemes on 3D electromagnetic problems.

2. Finite volume scheme for Maxwell's equations

Consider the propagation of electromagnetic waves in a three-dimensional heterogeneous linear isotropic medium with space-varying electric permittivity $\epsilon = \epsilon(\mathbf{x})$ and magnetic permeability $\mu = \mu(\mathbf{x})$. Given a bounded region $\Omega \subset \mathbb{R}^3$, the electric field $\mathbf{E}(\mathbf{x}, t)$ and the magnetic field $\mathbf{H}(\mathbf{x}, t)$ are governed by the system of Maxwell's equations

$$\begin{cases} \epsilon \frac{\partial \mathbf{E}}{\partial t} - \nabla \times \mathbf{H} = \mathbf{J}_E & \text{in } [0, T] \times \Omega, \\ \mu \frac{\partial \mathbf{H}}{\partial t} + \nabla \times \mathbf{E} = \mathbf{J}_H, & \text{in } [0, T] \times \Omega, \\ a\hat{\boldsymbol{n}} \times \mathbf{E} + b\hat{\boldsymbol{n}} \times (\hat{\boldsymbol{n}} \times \mathbf{H}) = 0 & \text{on } [0, T] \times \partial\Omega, \end{cases} \tag{1}$$

where $\mathbf{J}_E$ and $\mathbf{J}_H$ are the sources consisting of imposed currents and terms introduced by scattered field formulation, and $\hat{\boldsymbol{n}}$ is the outward unit normal of the boundary $\partial\Omega$. Parameters a and b define different boundary conditions:

- perfect electric conductor (PEC), $a = 1$ and $b = 0$,

- perfect magnetic conductor (PMC), $a = 0$ and $b = 1$, and

- Silver–Müller absorbing boundary condition, $a = 1$ and $b = \sqrt{\mu/\epsilon}$.

Consider the normalized quantities

$$x = l^{-1}\mathbf{x}, \qquad t = c_0 l^{-1}\mathbf{t}, \tag{2}$$

where l is a reference length and $c_0 = (\mu_0\epsilon_0)^{-1/2}$ is a dimensional speed of light in vacuum with $\epsilon_0 \approx 8.854 \cdot 10^{-12}\,\frac{\text{A}\cdot\text{s}}{\text{V}\cdot\text{m}}$ and $\mu_0 = 4\pi \cdot 10^{-7}\,\frac{\text{V}\cdot\text{s}}{\text{A}\cdot\text{m}}$. The fields $\mathbf{E}$ and $\mathbf{H}$ can be normalized to a typical electric field intensity E by

$$\boldsymbol{E} = \frac{\mathbf{E}}{E}, \qquad \boldsymbol{H} = \frac{Z_0}{E}\mathbf{H}, \qquad \boldsymbol{J}_E = \frac{lZ_0}{E}\mathbf{J}_E, \qquad \boldsymbol{J}_H = \frac{l}{E}\mathbf{J}_H, \tag{3}$$

where $Z_0 = \sqrt{\mu_0/\epsilon_0}$ is the dimensional free-space intrinsic impedance. Then the system (1) can be written in nondimensional form as

$$\begin{cases} \epsilon_r \frac{\partial \boldsymbol{E}}{\partial t} - \nabla \times \boldsymbol{H} = \boldsymbol{J}_E & \text{in } [0, c_0 l^{-1}T] \times \Omega, \\ \mu_r \frac{\partial \boldsymbol{H}}{\partial t} + \nabla \times \boldsymbol{E} = \boldsymbol{J}_H & \text{in } [0, c_0 l^{-1}T] \times \Omega, \\ a_r \hat{\boldsymbol{n}} \times \boldsymbol{E} + b_r \hat{\boldsymbol{n}} \times (\hat{\boldsymbol{n}} \times \boldsymbol{H}) = 0 & \text{on } [0, c_0 l^{-1}T] \times \partial\Omega, \end{cases} \tag{4}$$

where $\epsilon_r = \epsilon/\epsilon_0$, $\mu = \mu/\mu_0$, $a_r = a$, and $b_r = b/Z_0$. For a finite volume discretization, the first two equations of (4) are written in conservative form as

$$\boldsymbol{\alpha}\frac{\partial \boldsymbol{U}}{\partial t} + \nabla \cdot \boldsymbol{F}(\boldsymbol{U}) = \boldsymbol{J},$$

where

$$\boldsymbol{U} = \begin{bmatrix} \boldsymbol{H} \\ \boldsymbol{E} \end{bmatrix}, \qquad \boldsymbol{F}(\boldsymbol{U}) = [\boldsymbol{F}_1(\boldsymbol{U}), \boldsymbol{F}_2(\boldsymbol{U}), \boldsymbol{F}_3(\boldsymbol{U})]^T, \qquad \boldsymbol{F}_i = \begin{bmatrix} -e_i \times \boldsymbol{H} \\ e_i \times \boldsymbol{E} \end{bmatrix},$$

and

$$\boldsymbol{\alpha} = \begin{bmatrix} \epsilon_r & 0 \\ 0 & \mu_r \end{bmatrix}, \qquad \boldsymbol{J} = \begin{bmatrix} \boldsymbol{J}_E \\ \boldsymbol{J}_H \end{bmatrix}.$$

Consider a partition of the bounded domain $\Omega \subset \mathbb{R}^3$ into a tetrahedral mesh $\bar{\Omega}_T = \bigcup_{i=1}^N \bar{T}_i$. It is assumed that material properties are constant in each cell T_i. Integrating (4) over each tetrahedron T_i and defining the cell-averaged values of a given function u as $\bar{u}_i = (1/|T_i|)\int_{T_i} u\,dV$, the following semidiscrete finite volume scheme for Maxwell's equations is derived:

$$\boldsymbol{\alpha}_i \frac{\partial \bar{\boldsymbol{U}}_i}{\partial t} + \frac{1}{|T_i|}\int_{\partial T_i} \hat{\boldsymbol{n}} \cdot \boldsymbol{F}\,dS = \boldsymbol{\alpha}_i \frac{\partial \bar{\boldsymbol{U}}_i}{\partial t} + \frac{1}{|T_i|}\sum_{j=1}^4 |S_{ij}||\hat{\boldsymbol{n}} \cdot \boldsymbol{F}|_{S_{ij}} = \boldsymbol{J}_i, \tag{5}$$

where $\hat{\boldsymbol{n}}$ is the outward unit normal of the tetrahedron boundary ∂T_i consisting of four triangular surfaces S_{ij}, $j = 1, \ldots, 4$. Fluxes are computed using physical properties on elements T_i and T_j. Physical properties are the same inside a homogeneous medium and different on boundaries between dielectrics. To approximate the flux on each triangular surface S_{ij}, an upwind scheme based on the Steger–Warming

flux vector splitting [37] is used. Then a third-order linear scheme [40; 26] is used to approximate the field components.

3. Multirate Runge–Kutta methods in 1D

Consider the semidiscrete problem defined by the ODE

$$u_t = Lu \tag{6}$$

on some bounded region $\Omega \subset \mathbb{R}$ with a given initial value $u(0) = u^0$. Here the operator L represents the spatial approximation of the linear operator in the conservation law with some given order p. The computational domain is partitioned into two nonoverlapping subdomains $\Omega = D_1 \cup D_2 \cup \Gamma_{12}$, where D_1 has a fine mesh with size $h/2$ and D_2 has a coarse mesh with size h, and $\Gamma_{12} = \partial D_1 \cap \partial D_2$ is the boundary between D_1 and D_2. Assuming that the local time step satisfying the CFL condition on D_2 is Δt, then the local time step on D_1 is $\Delta t/2$. Denote by L_1 and L_2 two projections of the operator L onto domains D_1 and D_2, respectively; then we can split the right-hand side of (6) as

$$u_t = L_1 u + L_2 u. \tag{7}$$

For the analysis of multirate Runge–Kutta schemes it is convenient to consider their partitioned form (MPRK) [10; 23; 34]. The s-stage multirate Runge–Kutta method for (7) with two levels of refinement (local time steps) can be written as

$$u^{(i)} = u^n + \Delta t \sum_{k=1,2} \sum_{j=1}^{i-1} a_{ij}^{(k)} L_k u^{(j)}, \quad i = 1, \ldots, s, \tag{8}$$

$$u^{n+1} = u^n + \Delta t \sum_{k=1,2} \sum_{i=1}^{s} b_i^{(k)} L_k u^{(i)}. \tag{9}$$

It should be noted that the time-step factor is taken into account in the coefficients $a_{ij}^{(1)}$ and $a_{ij}^{(2)}$ and s is the number of MPRK stages. The scheme (8)–(9) is internally consistent if [23]

$$c_i^{(1)} = c_i^{(2)}, \qquad c_i^{(k)} = \sum_{j=1}^{s} a_{ij}^{(k)}, \quad i = 1, \ldots, s. \tag{10}$$

This condition ensures that the stage values on adjacent subdomains are consistent approximations to $u(t^n + c_i \Delta t)$. Failure to satisfy the internal consistency condition may lead to lower accuracy at interface points.

The accuracy of the MPRK schemes in the sense of a truncation error can be determined using the classic order conditions [21; 24; 1]. A few multirate schemes based on second-order Runge–Kutta methods satisfying second-order conditions

exist in literature [10; 38]. But generalizations of these schemes by using third-order base methods do not automatically generate a third-order MPRK method. The number of conditions quickly increases with order, and it becomes challenging to satisfy all of them. For linear problems, however, this number is reduced. For the third-order scheme the order conditions are given by the following lemma.

Lemma. *The multirate partitioned Runge–Kutta method* (8)–(9), *where* L_1 *and* L_2 *are linear constant-coefficient operators, is third-order accurate if the following order conditions are satisfied:*

$$\text{(first order)} \qquad (\boldsymbol{b}^{(k_1)})^T \mathbf{1} = 1, \qquad k_1, k_2 = 1, 2, \qquad (11)$$

$$\text{(second order)} \qquad (\boldsymbol{b}^{(k_1)})^T \boldsymbol{c}^{(k_2)} = \tfrac{1}{2}, \qquad k_1, k_2 = 1, 2, \qquad (12)$$

$$\text{(third order)} \qquad (\boldsymbol{b}^{(k_1)})^T \boldsymbol{A}^{(k_2)} \boldsymbol{c}^{(k_3)} = \tfrac{1}{6}, \quad k_1, k_2, k_3 = 1, 2. \qquad (13)$$

Proof. The proof is based on the estimate of the local truncation error $\tau^{n+1} = u^{n+1} - v(t^{n+1})$ after the time step Δt, where v is defined by

$$v_t = Lv, \quad v(t^n) = u^n.$$

Using Taylor series expansion for $v(t^{n+1})$ and substituting (8) into (9), the following expression for the truncation error is derived:

$$\tau^{n+1} = \Delta t \left[\sum_{k_1=1,2} (1 - (\boldsymbol{b}^{(k_1)})^T \mathbf{1}) L_{k_1} \right] v^n$$

$$+ \Delta t^2 \left[\sum_{k_1,k_2=1,2} \left(\tfrac{1}{2} - (\boldsymbol{b}^{(k_1)})^T \boldsymbol{c}^{(k_2)} \right) L_{k_1} L_{k_2} \right] v^n$$

$$+ \Delta t^3 \left[\sum_{k_1,k_2,k_3=1,2} \left(\tfrac{1}{6} - (\boldsymbol{b}^{(k_1)})^T \boldsymbol{A}^{(k_2)} \boldsymbol{c}^{(k_3)} \right) L_{k_1} L_{k_2} L_{k_3} \right] v^n + O(\Delta t^4).$$

The truncation error is $O(\Delta t^4)$ if the first three terms are zero. □

Now we consider two multirate schemes with a third-order SSP Runge–Kutta method as a base. The first scheme is an extension of the second-order scheme developed in [38] by Tang and Warnecke (MRK-TW). A generalization of their scheme for two time increments Δt and $\Delta t/2$ with an arbitrary base method $(\boldsymbol{A}, \boldsymbol{b}, \boldsymbol{c})$ is given in Table 1, where

$$\boldsymbol{A}_1 = [\boldsymbol{A}\hat{\boldsymbol{e}}_1, \, \mathbf{Z}_{s,s-1}], \qquad \boldsymbol{A}_2 = \boldsymbol{A} - \boldsymbol{A}_1, \qquad (14)$$

$$\boldsymbol{b}_1 = b_1 \hat{\boldsymbol{e}}_1, \quad \boldsymbol{b}_2 = \boldsymbol{b} - \boldsymbol{b}_1, \quad \hat{\boldsymbol{e}}_1 = [\underbrace{1, 0, \ldots, 0}_{s}]^T, \qquad (15)$$

and $\mathbf{Z}_{s,s-1}$ is the $s \times (s-1)$ zero matrix.

$$D_1: \quad \begin{array}{c|c} \boldsymbol{c}^{(1)} & \boldsymbol{A}^{(1)} \\ \hline & [\boldsymbol{b}^{(1)}]^T \end{array} \quad = \quad \begin{array}{c|cc} \frac{1}{2}\boldsymbol{c} & \frac{1}{2}\boldsymbol{A} & \\ \frac{1}{2}\mathbf{1}+\frac{1}{2}\boldsymbol{c} & \frac{1}{2}\boldsymbol{b}^T\otimes\mathbf{1} & \frac{1}{2}\boldsymbol{A} \\ \hline & \frac{1}{2}\boldsymbol{b}^T & \frac{1}{2}\boldsymbol{b}^T \end{array}$$

$$D_2: \quad \begin{array}{c|c} \boldsymbol{c}^{(2)} & \boldsymbol{A}^{(2)} \\ \hline & [\boldsymbol{b}^{(2)}]^T \end{array} \quad = \quad \begin{array}{c|cc} \frac{1}{2}\boldsymbol{c} & \frac{1}{2}\boldsymbol{A} & \\ \frac{1}{2}\hat{\boldsymbol{e}}_1+\boldsymbol{c} & \frac{1}{2}\boldsymbol{b}^T\otimes\hat{\boldsymbol{e}}_1+\boldsymbol{A}_1 & \boldsymbol{A}_2 \\ \hline & \boldsymbol{b}_1^T & \boldsymbol{b}_2^T \end{array}$$

Table 1. MPRK-TW scheme for arbitrary base method $(\boldsymbol{A}, \boldsymbol{b}, \boldsymbol{c})$ and time-step ratio 2.

Theorem. *The partitioned Runge–Kutta scheme defined by the Butcher tableau in Table 1 is internally consistent if*

$$\boldsymbol{c} = \mathbf{1} - \hat{\boldsymbol{e}}_1 \tag{16}$$

and is second-order accurate if the base method $(\boldsymbol{A}, \boldsymbol{b}, \boldsymbol{c})$ is at least second-order accurate and satisfies

$$b_1 = \tfrac{1}{2}. \tag{17}$$

Moreover, it has at most second-order accurate coupling regardless of the base method.

Proof. The proof of internal consistency is a straightforward application of the condition (10). Assuming that the base method $(\boldsymbol{A}, \boldsymbol{b}, \boldsymbol{c})$ satisfies the second-order conditions, the coupling conditions ((12), $k_1 \neq k_2$) applied to the scheme in Table 1 give us

$$b_i^{(1)} c_i^{(2)} = \tfrac{1}{2}\boldsymbol{b}^T\left(\tfrac{1}{2}\boldsymbol{c}+\tfrac{1}{2}\hat{\boldsymbol{e}}_1+\boldsymbol{c}\right) = \tfrac{3}{4}(\boldsymbol{b})^T\boldsymbol{c}+\tfrac{1}{4}b_1 = \tfrac{1}{2} \quad \Longleftrightarrow \quad b_1 = \tfrac{1}{2},$$

$$b_i^{(2)} c_i^{(1)} = (b_1\hat{\boldsymbol{e}}_1^T)\tfrac{1}{2}\boldsymbol{c}+(\boldsymbol{b}-b_1\hat{\boldsymbol{e}}_1)^T\left(\tfrac{1}{2}\mathbf{1}+\tfrac{1}{2}\boldsymbol{c}\right)$$

$$= \tfrac{1}{2}(\boldsymbol{b})^T\mathbf{1}-\tfrac{1}{2}b_1+\tfrac{1}{2}(\boldsymbol{b})^T\boldsymbol{c} = \tfrac{1}{2} \quad\quad\quad \Longleftrightarrow \quad b_1 = \tfrac{1}{2}.$$

Hence, the method is second-order accurate provided that $b_1 = \tfrac{1}{2}$. Assume that the base method $(\boldsymbol{A}, \boldsymbol{b}, \boldsymbol{c})$ is second-order accurate and also satisfies the third-order conditions for linear problems ((13), $k_1 = k_2 = k_3$). One of the linear coupling conditions in (13) with $k_1 = 1$ and $k_2 = k_3 = 2$ gives

$$(\boldsymbol{b}^{(1)})^T \boldsymbol{A}^{(2)} \boldsymbol{c}^{(2)} = \tfrac{1}{2}\boldsymbol{b}^T\tfrac{1}{2}\boldsymbol{A}\tfrac{1}{2}\boldsymbol{c}+\tfrac{1}{2}\boldsymbol{b}^T\left(\tfrac{1}{2}\boldsymbol{b}^T\otimes\hat{\boldsymbol{e}}_1+\boldsymbol{A}_1\right)\tfrac{1}{2}\boldsymbol{c}+\tfrac{1}{2}\boldsymbol{b}^T\boldsymbol{A}_2\left(\tfrac{1}{2}\hat{\boldsymbol{e}}_1+\boldsymbol{c}\right)$$

$$= \tfrac{1}{8}\boldsymbol{b}^T\boldsymbol{A}\boldsymbol{c}+\tfrac{1}{16}b_1+\tfrac{1}{2}\boldsymbol{b}^T\boldsymbol{A}\boldsymbol{c} = \tfrac{5}{48}+\tfrac{1}{16}b_1.$$

Therefore, the second- and third-order conditions cannot hold together. $\square$

It follows from the theorem that the partitioned Runge–Kutta scheme defined by the Butcher tableau in Table 1 is only first-order accurate with any third-order base method.

To get internal consistency for schemes of order $r > 2$, solutions on both sides of the interface Γ_{12} need to be adjusted. One strategy that provides higher-order coupling for linear problems was proposed in [27]. It is third-order accurate for third-order SSP Runge–Kutta base methods for linear problems (MRK-LLH).

For linear problems the Runge–Kutta method can be written as

$$\boldsymbol{u} = \boldsymbol{C}\boldsymbol{T}_{\Delta t}\boldsymbol{L}_s\boldsymbol{u}^n, \tag{18}$$

$$u^{n+1} = u^n + \boldsymbol{b}^T\boldsymbol{L}\boldsymbol{u}, \tag{19}$$

where

$$\boldsymbol{u} = [u^{(1)}, u^{(2)}, \ldots, u^{(s)}]^T, \qquad \boldsymbol{u}^n = [\underbrace{u^n, \ldots, u^n}_{s}]^T,$$

$$\boldsymbol{L}_s = \operatorname{diag}\{I, L, L^2, \ldots, L^{s-1}\}, \qquad \boldsymbol{L} = \operatorname{diag}\{\underbrace{L, L, \ldots, L}_{s}\},$$

$$\boldsymbol{C} = \begin{bmatrix} 1 & 0 & 0 & \cdots & 0 \\ 1 & a_{21} & 0 & \cdots & 0 \\ 1 & \sum a_{3j} & a_{32}a_{21} & \cdots & 0 \\ \vdots & \vdots & \vdots & \ddots & \vdots \\ \vdots & \vdots & \vdots & \ddots & 0 \\ 1 & \sum a_{sj} & \sum a_{sj}a_{jk} & \cdots & a_{s,s-1}\cdots a_{21} \end{bmatrix} \tag{20}$$

and

$$\boldsymbol{T}_{\Delta t} = \operatorname{diag}\{1, \Delta t, \ldots, \Delta t^{s-1}\}. \tag{21}$$

Since for the linear case we have

$$L^i u|_{t=t^n} = \left.\frac{d^i u}{dt^i}\right|_{t=t^n}, \tag{22}$$

therefore the RK stage values $\boldsymbol{u}$ can be written in terms of time derivatives of u^n.

Now consider the partition $\Omega = D_1 \cup D_2 \cup \Gamma_{12}$ defined by the local time steps $\Delta t_1 = \Delta t/2$, and $\Delta t_2 = \Delta t$. First the solution is advanced on both subdomains from $t = t^n$ with their local time steps Δt_1 and Δt_2. The stage values at the time level t^n inside of each subdomain are computed by

$$\boldsymbol{u}_k = \boldsymbol{C}\boldsymbol{T}_{\Delta t_k}\boldsymbol{d}\boldsymbol{u}^n, \quad k = 1, 2, \tag{23}$$

where

$$\boldsymbol{d}\boldsymbol{u}^n = \left[u, \frac{du}{dt}, \frac{d^2u}{dt^2}, \ldots, \frac{d^{s-1}u}{dt^{s-1}}\right]^T_{t=t^n}. \tag{24}$$

To calculate the fluxes on the interface Γ_{12} the stage values $\tilde{\boldsymbol{u}}_1$ and $\tilde{\boldsymbol{u}}_2$ are needed for time advancing from $t = t^n$ on D_2 and D_1, respectively. Using (23) the stages

$$D_1: \quad \begin{array}{c|c} \boldsymbol{c}^{(1)} & \boldsymbol{A}^{(1)} \\ \hline & [\boldsymbol{b}^{(1)}]^T \end{array} \quad = \quad \begin{array}{c|cc} \frac{1}{2}\boldsymbol{c} & \frac{1}{2}\boldsymbol{A} & \boldsymbol{0} \\ \frac{1}{2}\boldsymbol{1}+\frac{1}{2}\boldsymbol{c} & \frac{1}{2}\boldsymbol{b}^T \otimes \boldsymbol{1} & \frac{1}{2}\boldsymbol{A} \\ \hline & \frac{1}{2}\boldsymbol{b}^T & \frac{1}{2}\boldsymbol{b}^T \end{array}$$

$$D_2: \quad \begin{array}{c|c} \boldsymbol{c}^{(2)} & \boldsymbol{A}^{(2)} \\ \hline & [\boldsymbol{b}^{(2)}]^T \end{array} \quad = \quad \begin{array}{c|cc} \frac{1}{2}\boldsymbol{c} & \frac{1}{2}\boldsymbol{A} & \boldsymbol{0} \\ \boldsymbol{q} & \boldsymbol{Q} & \boldsymbol{0} \\ \hline & \boldsymbol{b}^T\boldsymbol{G}^{(1)} & \boldsymbol{0} \end{array}$$

Table 2. MPRK-LLH scheme for arbitrary base method $(\boldsymbol{A}, \boldsymbol{b}, \boldsymbol{c})$ and time-step ratio 2.

$\tilde{\boldsymbol{u}}_1$ and $\tilde{\boldsymbol{u}}_2$ are obtained using the coupling [27]

$$[\tilde{\boldsymbol{u}}_1]_{t^n} = \boldsymbol{C}\boldsymbol{T}_{\Delta t_2}d\boldsymbol{u}^n = \boldsymbol{C}\boldsymbol{T}_{\Delta t_2}\boldsymbol{T}_{\Delta t_1}^{-1}\boldsymbol{C}^{-1}\boldsymbol{u}_1 = \boldsymbol{G}^{(1)}\boldsymbol{u}_1, \tag{25}$$

$$[\tilde{\boldsymbol{u}}_2]_{t^n} = \boldsymbol{C}\boldsymbol{T}_{\Delta t_1}d\boldsymbol{u}^n = \boldsymbol{C}\boldsymbol{T}_{\Delta t_1}\boldsymbol{T}_{\Delta t_2}^{-1}\boldsymbol{C}^{-1}\boldsymbol{u}_2 = \boldsymbol{G}^{(2)}\boldsymbol{u}_2. \tag{26}$$

Matrices $\boldsymbol{G}^{(1)}$ and $\boldsymbol{G}^{(2)}$ are lower triangular and have the properties

$$\boldsymbol{G}^{(1)}\boldsymbol{G}^{(2)} = \boldsymbol{G}^{(2)}\boldsymbol{G}^{(1)} = \boldsymbol{I}_s, \tag{27}$$

$$\sum_{j=1}^{s} G_{ij}^{(1)} = \sum_{j=1}^{s} G_{ij}^{(2)} = 1, \tag{28}$$

$$\boldsymbol{G}^{(1)}\tilde{\boldsymbol{u}}_2 = \boldsymbol{u}_2, \qquad \boldsymbol{G}^{(2)}\tilde{\boldsymbol{u}}_1 = \boldsymbol{u}_1. \tag{29}$$

At the second step the solution is advanced on the fine mesh only using coupling stage values $\tilde{\boldsymbol{u}}_2$ at the time level $t = t^n + \Delta t_1$ computed by [27]

$$[\tilde{\boldsymbol{u}}_2]_{t^n+\Delta t_1} = \boldsymbol{C}\boldsymbol{T}_{\Delta t_1}\boldsymbol{H}_{\Delta t_1}\boldsymbol{T}_{\Delta t_2}^{-1}\boldsymbol{C}^{-1}\boldsymbol{u}_2 =: \boldsymbol{K}\boldsymbol{u}_2, \tag{30}$$

where

$$\boldsymbol{H}_{\Delta t} = \begin{bmatrix} 1 & \Delta t & \Delta t^2/2 & \cdots & \Delta t^{s-1}/(s-1)! \\ 0 & 1 & \Delta t & \cdots & \Delta t^{s-2}/(s-2)! \\ 0 & 0 & 1 & \cdots & \Delta t^{s-3}/(s-3)! \\ \vdots & \vdots & \vdots & \ddots & \vdots \\ 0 & 0 & 0 & \cdots & 1 \end{bmatrix}. \tag{31}$$

The MRK-LLH method described above can be written in the Butcher tableau form shown in Table 2, where

$$\boldsymbol{Q} = \boldsymbol{K}\boldsymbol{A}\boldsymbol{G}^{(1)}, \tag{32}$$

and $\boldsymbol{q} = [q_1, \ldots, q_s]^T$, with

$$q_i = \sum_{j=1}^{s} Q_{ij} = \sum_{j=1}^{s-1}\left(\sum_{k=j+1}^{s}\sum_{l=j}^{k-1} K_{ik}a_{kl}G_{lj}^{(1)}\right). \tag{33}$$

Consistency and accuracy analysis for the MPRK-LLH scheme can be summarized by the following theorem.

Theorem. *The partitioned Runge–Kutta scheme defined by the Butcher tableau in Table 2 is internally consistent and third-order accurate with three-stage SSP RK3 schemes for linear problems.*

Proof. The scheme is internally consistent by design. It can be shown by verifying the condition

$$q = \tfrac{1}{2}\mathbf{1} + \tfrac{1}{2}c. \tag{34}$$

It also follows from the application of the order conditions (11)–(13) that the scheme MPRK-LLH is third-order accurate for three-stage RK3 base methods for linear problems. □

The extension of the scheme to any arbitrary time-step ratio is straightforward [27]. To update stage values the following general coupling expressions replace (25)–(26) and (30):

$$[\tilde{\boldsymbol{u}}_1]_{t^{n,k_2}} = \boldsymbol{K}^{(1)}_{\Delta t_{k_2,k_1}}[\boldsymbol{u}_2]_{t^{n,k_1}}, \quad \boldsymbol{K}^{(1)}_{\Delta t_{k_2,k_1}} = \boldsymbol{C}\boldsymbol{T}_{\Delta t_2}\boldsymbol{H}_{\Delta t_{k_2,k_1}}\boldsymbol{T}^{-1}_{\Delta t_1}\boldsymbol{C}^{-1}, \tag{35}$$

$$[\tilde{\boldsymbol{u}}_2]_{t^{n,k_2}} = \boldsymbol{K}^{(2)}_{\Delta t_{k_2,k_1}}[\boldsymbol{u}_1]_{t^{n,k_1}}, \quad \boldsymbol{K}^{(2)}_{\Delta t_{k_2,k_1}} = \boldsymbol{C}\boldsymbol{T}_{\Delta t_1}\boldsymbol{H}_{\Delta t_{k_2,k_1}}\boldsymbol{T}^{-1}_{\Delta t_2}\boldsymbol{C}^{-1}. \tag{36}$$

In the next section we present the steps to implement both schemes on 3D meshes with arbitrary time-step ratios.

4. MRK scheme in 3D

Consider a semidiscrete system of Maxwell's equations (5) written as

$$\boldsymbol{U}_t = \boldsymbol{L}\boldsymbol{U}, \tag{37}$$

and defined on a computational domain with mesh $\bar{\Omega}_T = \bigcup_{i=1}^{N}\bar{T}_i$. This domain is partitioned into K multirate groups of elements $\bar{\Omega}_T = \bigcup_{k=1}^{K}\overline{D^{(k)}}$ using a local stability criterion. Let $\{\Delta\tau_i\}_{i=1}^{N}$ be a set of characteristic stable time steps obtained by [7]

$$\Delta\tau_i \leq \frac{|T_i|}{c_i \sum_{j\in\mathscr{I}_i}|S_{ij}|}, \tag{38}$$

for each cell T_i with volume $|T_i|$, where $\mathscr{I}_i$ is the set of indexes of neighboring elements, and $|S_{ij}|$ is the area of the face shared by element T_i and its j-th neighbor. Let $\Delta t_{\min} = \min_i\{\Delta\tau_i\}$ and $\Delta t_{\max} = \max_i\{\Delta\tau_i\}$. Each time step Δt_k can be defined as a product of $\Delta t_{\min}$ and some rational number $0 \leq p_k \leq \Delta t_{\max}/\Delta t_{\min}$. Then K multirate groups can be defined as

$$D^{(k)} = \begin{cases} \{T_i \in \Omega, \ \Delta\tau_i \in [\Delta t_k, \Delta t_{k+1})\}, & k = 1, \ldots, K-1, \\ \{T_i \in \Omega, \ \Delta\tau_i \in [\Delta t_k, \Delta t_{\max})\}, & k = K. \end{cases} \tag{39}$$

Each multirate group consists of elements of bulk group $D^{(k)}_{\text{bulk}}$ and inner buffer group $D^{(k)}(0)$. Bulk group $D^{(k)}_{\text{bulk}}$ includes all elements of $D^{(k)}$ that are sufficiently far from the boundary $\Gamma_k = \partial D^{(k)} \cap \left(\bigcup_{l=1,\, l \neq k}^{K} \partial D^{(l)} \right)$; therefore, time integration on these elements does not depend on values from neighboring multirate groups. The size of the inner buffer $D^{(k)}(0)$ depends on the order of finite volume approximation and consists of elements of $D^{(k)}$ nearest to Γ_k for which time integration involves values from adjacent multirate groups. In addition to bulk and inner buffer groups we need to define outer buffer groups, where the values of adjacent multirate groups are updated to ensure proper coupling. Let Δt be the global time step, at which the solution in all multirate groups is synchronized, and the final time is achieved after N^t global time integrations, i.e., $T = N^t \Delta t$. Assuming that each global time step from t^n to t^{n+1} consists of m local multirate stages, we associate to each multirate group $D^{(k)}$ the local time $t_k^{n,l}$, $l \in \{1, \ldots, m\}$, at the l-th multirate stage. The global time $t^{n,l}$ is defined by local times $t_k^{n,l}$, and its definition depends on the multirate scheme.

The most common definition of local time steps [15; 29; 31; 35] is given by

$$\{\Delta t_k\}_{k=1}^{K_2} = \{2^{k-1} \Delta t_{\text{min}}\}_{k=1}^{K_2}, \quad K_2 = \left\lfloor \log_2 \frac{\Delta t_{\text{max}}}{\Delta t_{\text{min}}} \right\rfloor + 1.$$

Another set of factors $\{p_k\}_{k=1}^{K}$ that we found to give better distribution of local time steps is given by

$$\{p_k\}_{k=1}^{K} = \{K / k \Delta t_{\text{min}}\}_{k=0}^{K},$$

where

$$K = \left\lfloor \frac{\Delta t_{\text{max}}}{\Delta t_{\text{min}}} \right\rfloor. \tag{40}$$

This partition is then optimized by varying the parameters Δt_{min} and κ and removing unnecessary groups. We will refer to this partition as optimized partition (OP). The outline of the optimization procedure is the following:

(1) Using the values of Δt_{min} and K defined by (40) we introduce two parameters for the new multirate partition

$$\Delta t^*_{\text{min}} = \alpha \Delta t_{\text{min}}, \quad \alpha \in [0.8, 1], \tag{41}$$

$$K^* = \beta K, \quad \beta \in [0.8, 1.2]. \tag{42}$$

It should be noted that broader ranges of values for the parameters α and β introduced too many local minima (and repeating time-step distributions) for the optimization procedure to be efficient.

(2) For a randomly chosen pair $(\Delta t^*_{\text{min}}, K^*)$ using a certain search procedure,

(a) construct a multirate partition;

    (b) remove unnecessary multirate groups: if a subdomain with Δt_k consists of a few isolated elements, add it to the subdomain with Δt_{k-1}; and

    (c) estimate theoretical speedup from the resulting partition.

(3) Go to step 2 if the convergence criterion is not satisfied. If converged, take the best estimated partition as the final choice.

In the present work an improved controlled random search algorithm by [28] was used as a searching procedure. It was run once before the simulation with a limit of 200 iterations, and usually took around 30 iterations to converge. The final partition is defined by the optimal pair $(\Delta t_{\min}^*, K^*)$ and after merging of unnecessary MRK groups has the total number of multirate groups $\leq K^*$. The convergence criterion is based on the theoretical speedup formula given by

$$S = \frac{\Delta t_{\min}^{-1} s N}{\sum_{k=1}^{K} \Delta t_k^{-1} s N_{D^{(k)}}}, \tag{43}$$

where N is the total number of mesh elements, s is the number of Runge–Kutta stages, and $N_{D^{(k)}}$ is the number of elements in the $D^{(k)}$ multirate group. During the initialization, the local time-step partition is computed and subdomains are determined. Multirate partitions are defined so that all local times $t_k^{n,l}$ are synchronized at some global time step Δt. As a result the computational process can be divided into N blocks with global time step Δt. In this work only static meshes were used in simulations. The same idea for multirate partitioning can be applied to dynamic mesh refinement. In this case, multirate groups have to be defined for each mesh refinement at minimum computational cost.

4.1. *Tang–Warnecke scheme.* The coupling in the MR-TW scheme is done by projecting the solution using the Runge–Kutta step in the adjacent multirate group. Therefore, with three-stage RK3 base scheme the outer buffer consists of three-stage coupling groups $D^{(k)}(q)$, $q = 1, \ldots, 3$.

    Consider the partition into K multirate groups with time steps Δt_k defined by any partition method. Let m be the number of local time updates from $t^n = t^{n,0}$ to $t^{n+1} = t^n + \Delta t = t^{n,m}$ at which all multirate groups are synchronized. Local times $t_k^{n,l}$, $1 \leq l \leq m$, are updated at the beginning of the time cycle by

$$t_k^{n,l} = \begin{cases} t_k^{n,l-1} + \Delta t_k & \text{if } t_k^{n,l-1} = t^{n,l-1}, \\ t_k^{n,l-1} & \text{if } t_k^{n,l-1} > t^{n,l-1}. \end{cases} \tag{44}$$

Then the global time corresponding to the l-th multirate stage is obtained by

$$t^{n,l} = \min_k t_k^{n,l}. \tag{45}$$

At the beginning of each multirate stage l the initial stage values are given by

$$W^{(1)} = \begin{cases} U_k^{n,l-1} & \text{on } D^{(k)}, \\ U_j^{n,l^*} & \text{on } \bigcup_{j=1, j \neq k}^{K} \left(D^{(j)} \cap \left(\bigcup_{r=1}^{s} D^{(k)}(r) \right) \right). \end{cases} \tag{46}$$

Here $l^* \leq l-1$ is the last multirate stage with $t_k^{n,l^*} = t_j^{n,l^*}$. The q-th stage value of the Runge–Kutta scheme on multirate groups $D^{(k)}$ is then computed by

$$U_k^{(q)} = U_k^{n,l-1} + \Delta t_k \sum_{r=1}^{q-1} a_{qr} L_k W^{(r)}, \quad q = 2, \dots, s, \tag{47}$$

and coupling values denoted by $V_j^{(q)}$ are computed in the outer buffer of $D^{(k)}$ by

$$V_j^{(q)} = U_j^{n,l^*} + \Delta t_{k,j} \sum_{r=1}^{q-1} a_{qr} L_j W^{(r)}, \tag{48}$$

where $\Delta t_{k,j} = t_k^{n,l} - t_j^{n,l^*}$ and

$$W^{(q)} = \begin{cases} U_k^{(q)} & \text{on } D^{(k)}, \\ V_j^{(q)} & \text{on } \bigcup_{j=1, j \neq k}^{K} \left(D^{(j)} \cap \left(\bigcup_{r=1}^{s+1-q} D^{(k)}(r) \right) \right), \end{cases} \quad q = 2, \dots, s.$$

4.2. Liu–Li–Hu linear scheme.
The coupling in the MRK-LLH is done by modifying the latest stage values in cells closest to the multirate interface. The outer buffer includes only one coupling group $D^k(1)$.

Consider a partition into K multirate groups with time steps Δt_k and m local time updates from $t^n = t^{n,0}$ to $t^{n+1} = t^n + \Delta t = t^{n,m}$. Local times $t_k^{n,l}$, $l \in \{0, \dots, m-1\}$, associated with each multirate group $D^{(k)}$ are updated at the end of the l-th stage by

$$t_k^{n,l+1} = \begin{cases} t_k^{n,l} + \Delta t_k & \text{if } t_k^{n,l} + \Delta t_k = t^{n,l+1}, \\ t_k^{n,l} & \text{if } t_k^{n,l} + \Delta t_k > t^{n,l+1}, \end{cases} \tag{49}$$

where

$$t^{n,l+1} = \min_k (t_k^{n,l} + \Delta t_k). \tag{50}$$

At each multirate stage l for every $D^{(k)}$ with $t_k^{n,l} = t^{n,l}$ the coupling RK stage values V_j are computed in the outer buffer $\bigcup_{j=1, j \neq k}^{K} (D^{(j)} \cap D^{(k)}(1))$ by

$$V_j^{(q)} = \begin{cases} \sum_{r=1}^{q} [C T_{\Delta t_j} T_{\Delta t_k}^{-1} C^{-1}]_{qr} U_j^{(r)} & \text{if } t_j^{n,l} = t_k^{n,l}, \\ \sum_{r=1}^{s} [C T_{\Delta t_j} H_{\Delta t_{k,j}^{n,l}} T_{\Delta t_k}^{-1} C^{-1}]_{qr} U_j^{(r)} & \text{if } t_j^{n,l} < t_k^{n,l}, \end{cases} \tag{51}$$

where $\Delta t_{k,j}^{n,l} = t_k^{n,l} - t_j^{n,l}$, $U_j^{(r)}$ are the RK stage values on $D^{(j)}$ at $t_j^{n,l}$, and matrices C, $T_{\Delta t}$, and $H_{\Delta t}$ are defined by (20), (21), and (31), respectively. Then the time integration is performed on $D^{(k)}$. There are no additional RK steps in the outer

buffer, since the coupling values are defined by (51). Therefore, in this algorithm we avoid additional costly computations of fluxes in the outer buffer.

5. Numerical experiments

All numerical experiments were completed with double precision on a computer with a four-core Intel i7-4790K CPU. The computational code of the finite volume engine was written in C++ with OpenMP and compiled using GCC. Tetrahedral meshes for all 3D problems considered in this work were generated using the open source software Gmsh version 2.7.1. As was mentioned in Section 4, the MRK3-TW scheme requires more flux computations while MRK3-LLH uses more coupling steps. To assess schemes' efficiency, in our numerical experiments we compared both CPU time and the total number of flux computations for single-rate RK3 and multirate schemes. Flux computation is the most computationally expensive operation and for large meshes it takes over 90% of CPU time (94% in the example on page 83). At the same time, on small meshes with large time-step ratio this percentage is lower and the speedup of MRK3-LLH compared to the RK3-TW scheme is diminished with too many coupling steps. Therefore, in some examples RK3-TW slightly outperforms MRK3-LLH in terms of CPU time.

Example (1D linear advection equation). Consider the linear advection problem

$$u_t + u_x = 0, \quad x \in \Omega = (-1, 1), \tag{52}$$

$$u(x, 0) = \sin(\pi x), \tag{53}$$

with periodic boundary conditions. The computational domain consists of two subdomains $D_1 = (-1, 0)$ with grid size $h/2$, and $D_2 = (0, 1)$ with grid size h. For the space approximation a finite volume scheme based on a third-order WENO reconstruction [25] is employed. Convergence results for MRK3-TW and MRK3-LLH are compared to the ones by the non-MRK SSP RK3 scheme on a uniform grid (see Table 3).

Example (PEC sphere). Consider the classical scattering problem of a plane wave at a PEC sphere for which the analytic series solution is known [22; 5]. The computational domain is represented by a sphere of radius 3 m with a sphere (PEC) of radius 0.5 m cut out at the origin. The x component of the electric field of the incident plane wave E_x^I is given by the derivative of the Gaussian pulse:

$$E_x^I = -2\frac{t - t_0}{b^2}Ae^{-(t-t_0)^2/b^2}, \tag{54}$$

where $A = 1.7489 \times 10^{-9}\ \frac{\text{V·s}}{\text{m}}$, $b = 1.5 \times 10^{-9}$ s, and $t_0 = 6 \times 10^{-9}$ s.

The average linear cell size near the PEC surface is 0.0225 m, and on the outer boundary of the domain it is 0.15 m. The resulting nonuniform mesh has linear

	RK3		MRK3-TW		MRK3-LLH	
h^{-1}	$l_2(u)$	$r_2(u)$	$l_2(u)$	$r_2(u)$	$l_2(u)$	$r_2(u)$
100	9.006×10^{-6}		3.895×10^{-3}		1.086×10^{-5}	
200	1.126×10^{-6}	3.00	1.963×10^{-3}	0.99	1.357×10^{-6}	3.00
400	1.407×10^{-7}	3.00	9.863×10^{-4}	0.99	1.695×10^{-7}	3.00
800	1.759×10^{-8}	3.00	4.945×10^{-4}	1.00	2.118×10^{-8}	3.00
1 600	2.198×10^{-9}	3.00	2.477×10^{-4}	1.00	2.647×10^{-9}	3.00
3 200	2.751×10^{-10}	3.00	1.240×10^{-4}	1.00	3.310×10^{-10}	3.00
6 400	3.507×10^{-11}	2.97	6.203×10^{-5}	1.00	4.170×10^{-11}	2.99

Table 3. Convergence of RK3 and MRK3 schemes for the linear advection equation with initial data $u(x, 0) = \sin(\pi x)$ at $T = 1$. Here $r_2(u) = \log_2(l_2(u^{[h]})/l_2(u^{[h/2]}))$.

P2 partition

OP partition

Multirate domains:

$\Delta t_{\min}$: 199
$2\Delta t_{\min}$: 111412
$4\Delta t_{\min}$: 28267
$8\Delta t_{\min}$: 30531
$16\Delta t_{\min}$: 261002

Multirate domains with
$\Delta t^*_{\min} = 0.8\Delta t_{\min}$:

$\Delta t^*_{\min}$: 1
$41/32\Delta t^*_{\min}$: 7
$41/24\Delta t^*_{\min}$: 227
$41/16\Delta t^*_{\min}$: 90428
$41/8\ \Delta t^*_{\min}$: 42913
$41/4\ \Delta t^*_{\min}$: 17932
$41/2\ \Delta t^*_{\min}$: 279903
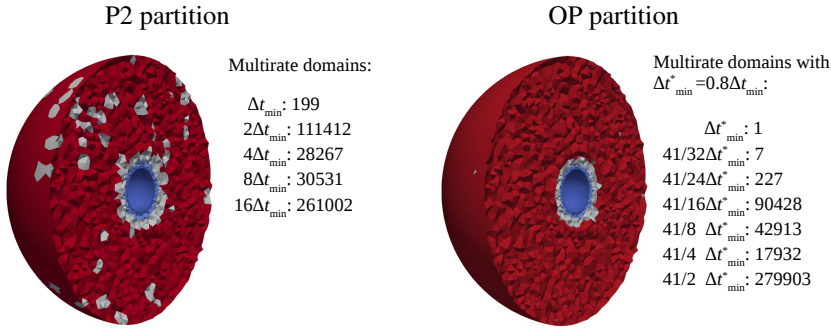
Figure 1. Scattering from PEC sphere: multirate domain partition for the mesh with linear cells size ratio 1 : 6.667.

cell-size ratio 1 : 6.667, and consists of 431 411 tetrahedra with 14 374 of them containing a PEC face. Two types of partitions used in our experiments with the MRK3-TW and MRK3-LLH schemes are shown of Figure 1. The time-domain solutions for the electric field at a side-scatter observation point by two MRK3 schemes and single-rate RK3 are shown in Figure 2. The maximum errors at four observation points are shown in Table 4. The error plots in Figure 2 show that the same accuracy is obtained with the MRK3-LLH-OP scheme as with the single-rate RK3 method. At the same time, the error of the solution obtained by the MRK3-TW-OP scheme is much larger. This demonstrates only first-order accuracy of the MRK3-TW scheme as in 1D analysis. The same conclusions can be drawn from the errors presented in Table 4. A comparison of numerical efficiency for both multirate schemes against the single-rate RK3 is shown in Table 5. While both schemes have faster CPU time than a single-rate scheme, in this example, CPU performance of the MRK3-LLH scheme is higher due to fewer interface flux computations required. It should be noted that P2 partition uses the largest time step as Δt_g, and in OP
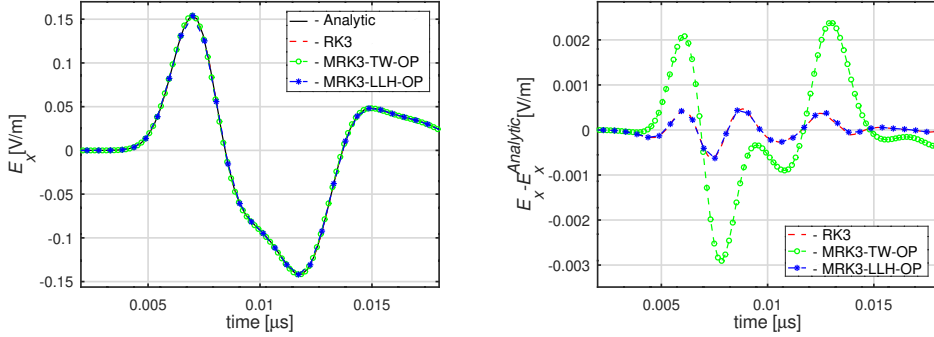
Figure 2. Scattering from PEC sphere: time-domain solution at side-scatter observation point $(-1.15, 0, 0)$ using RK3 and MRK3 schemes.

scheme	side-scatter $(1.15, 0, 0)$	side-scatter $(-1.15, 0, 0)$	forward-scatter $(0, 0, 1.15)$	back-scatter $(0, 0, -1.15)$
RK3	1.1842×10^{-3}	1.1788×10^{-3}	8.2511×10^{-3}	3.1686×10^{-3}
MRK3-TW-P2	2.3026×10^{-3}	3.2627×10^{-3}	1.3442×10^{-2}	5.4663×10^{-3}
MRK3-TW-OP	2.2546×10^{-3}	2.8729×10^{-3}	1.3193×10^{-2}	5.5634×10^{-3}
MRK3-LLH-P2	1.1519×10^{-3}	9.3847×10^{-4}	8.0727×10^{-3}	3.1817×10^{-3}
MRK3-LLH-OP	1.2615×10^{-3}	1.2559×10^{-3}	7.8927×10^{-3}	3.1663×10^{-3}

Table 4. PEC sphere: $\max_n |E_x(t^n) - E_x^{\text{Analytic}}(t^n)|$ at observation points for RK3 and MRK3.

scheme	# of Δt_g	$n(LU)$	$\frac{n(LU)_{RK3}}{n(LU)}$	CPU [ms]	$\frac{CPU_{RK3}}{CPU}$
RK3	7 245	9 376 718 085	1	6 498 449	1
MRK3-TW-P2	453	2 325 701 094	4.03	1 893 579	3.43
MRK3-TW-OP	221	2 182 108 032	4.3	1 986 033	3.27
MRK3-LLH-P2	453	2 062 756 791	4.55	1 587 369	4.09
MRK3-LLH-OP	230	1 944 214 380	4.82	1 586 064	4.1

Table 5. PEC sphere: performance of MRK3 schemes compared to single-rate RK3 for domain partitions shown on Figure 1, here $n(LU)$ is the number of flux operations which is the most computationally expensive operation.

partition Δt_g (time step to synchronize solutions across multirate domains) is twice as large as the largest time step (see Figure 1). Therefore, the number of Δt_g steps in Table 5 is equivalent to the number of synchronization steps, not the number of largest time steps.

Example (parallel-plate waveguide). A parallel-plate waveguide is represented by a cubic domain with two faces parallel to the xy-plane being PEC plates, and two faces parallel to the zx-plane being PMC plates. A plane-wave excited on the port
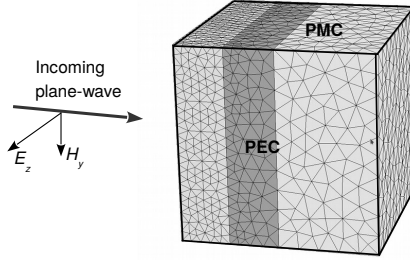
Figure 3. Parallel-plate waveguide: geometry and mesh.

	RK3		MRK3-TW		MRK3-LLH	
# of cells	L^2 error	order	L^2 error	order	L^2 error	order
8 040	6.824139×10^{-3}		1.929949×10^{-2}		6.890073×10^{-3}	
64 076	9.177931×10^{-4}	2.89	8.110855×10^{-3}	1.25	9.246888×10^{-4}	2.9
554 668	1.107034×10^{-4}	3.05	4.385090×10^{-3}	0.89	1.112703×10^{-4}	3.05

Table 6. Parallel-plate waveguide: L^2 errors at $T = l c_0^{-1}$ ($l = 2$ m) using RK3 and MRK3 schemes.

$x = -1$ and propagating in the x-direction is given by

$$E_z^{\text{in}} = f(t), \qquad H_y^{\text{in}} = -f(t)\sqrt{\epsilon/\mu}, \qquad E_x^{\text{in}} = E_y^{\text{in}} = H_x^{\text{in}} = H_z^{\text{in}} = 0, \quad (55)$$

where $f(t)$ is defined by the Gaussian pulse

$$f(t) = e^{-(t-t_0)^2/b^2}, \quad b = 1.2 \times 10^{-9} \text{ [s]}, \ t_0 = c_0^{-1} \text{ [s]}. \tag{56}$$

Experiments are performed on three meshes with fine mesh linear size Δx equal to 0.025, 0.05, and 0.1 m, and coarse mesh size $2\Delta x$. An example of problem geometry and mesh is shown in Figure 3. Convergence results are presented in Table 6. On each mesh we compute the L^2 error at time $T = 2c_0^{-1}$ by

$$l_2(\boldsymbol{U}(T)) = \frac{\left[\sum_{i=1}^{N}|T_i| \sum_{j=1}^{3} \frac{1}{2}(\epsilon_r \epsilon_0 (\bar{E}_i^j)^2 + \mu_r \mu_0 (\bar{H}_i^j)^2)\right]^{1/2}}{\left[\epsilon_0 \sum_{i=1}^{N}|T_i|\right]^{1/2}}. \tag{57}$$

In another experiment, an inhomogeneous mesh with linear cell-size ratio $1 : 160$ was generated similar to the example from [15]. The plane wave (55) uses the pulse given as one wavelength of a cosine function

$$f(t) = \tfrac{1}{2}(1 + \cos(2\pi c_0(t - t_0)))\theta(t - t_s)\theta(t_e - t), \tag{58}$$

where $t_0 = 0.54 c_0^{-1}$ [s], $t_s = 1.04 c_0^{-1}$ [s], $t_e = 2.04 c_0^{-1}$ [s], and $\theta(t)$ is the Heaviside function. A schematic representation of the geometry and resulting mesh are shown
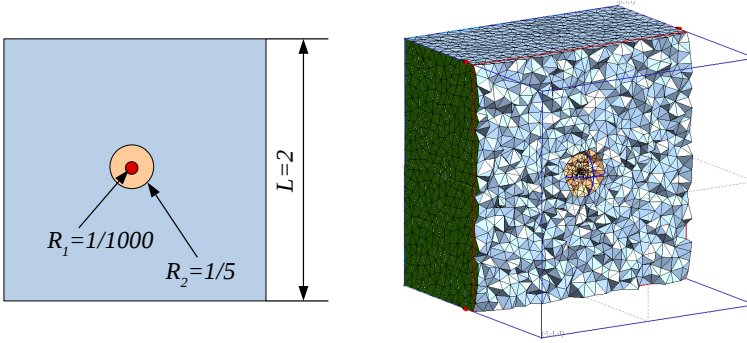
Figure 4. Parallel-plate waveguide: inhomogeneous mesh with linear cell-size ratio 1 : 160.

scheme	# of Δt_g	$n(LU)$	$\frac{n(LU)_{\text{RK3}}}{n(LU)}$	CPU [ms]	$\frac{\text{CPU}_{\text{RK3}}}{\text{CPU}}$	L^2 error
RK3	51 978	13 180 477 284	1	9 130 297	1	5.7813×10^{-3}
MRK3-TW-P2	204	232 562 448	56.68	296 687	30.77	1.3733×10^{-2}
MRK3-TW-OP	136	189 863 344	69.42	271 379	33.64	1.2976×10^{-2}
MRK3-LLH-P2	204	231 063 048	57.04	378 350	24.13	5.6292×10^{-3}
MRK3-LLH-OP	136	173 453 040	75.99	366 928	24.88	5.7684×10^{-3}

Table 7. Parallel-plate waveguide with mesh-size ratio 1 : 160: performance of MRK3 schemes compared to single-rate RK3.

in Figure 4. The region defined by a sphere with radius R_1 has the smallest elements with linear size $R_1/1.6$. Area between spheres with radii R_1 and R_2 provide gradual transition to the coarsest mesh with average linear cell size 0.1. The resulting mesh has linear cell-size ratio 1 : 160 and contains 84 526 tetrahedra with fewer than 200 of elements of the smallest size. Using the P2 partition, the computational domain is divided into 9 multirate groups with the maximum time-step ratio 1 : 256. In this partition 0.12% of elements belong to multirate group with the smallest time step Δt_{min} and 86% to the group with time step $128\Delta t_{\text{min}}$. OP partition divides the computational domain into 10 multirate groups with time step ratio 1 : 192 and global synchronization time step $384\Delta t_{\text{min}}^*$. In this partition 0.14% of elementsbelong to the multirate group with the smallest time step Δt_{min}^* and 95.6% to the group with time step $192\Delta t_{\text{min}}^*$. Numerical speedup achieved by the MRK3-TW and MRK3-LLH schemes is presented in Table 7. The results demonstrate greater speedup than in [15] even with the third-order scheme where coupling is more expensive due to the flexibility in time-step ratio. Speedup achieved by MRK3-TW is noticeably higher in this example. It can be explained by the fact that this test case uses a small mesh and the weight of additional flux computations needed for coupling in MRK3-TW turns out to be less costly than higher-order coupling used in MRK3-LLH.

R=12.5 mm
b=6.5 mm
r_1=0.63 mm
r_2=2.25 mm
l_p=6.5 mm
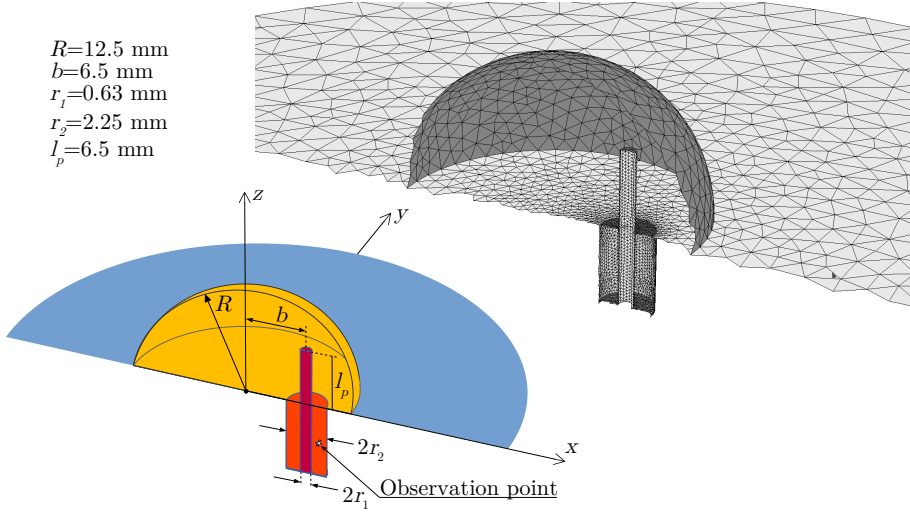
Figure 5. DRA: geometry and mesh.

Example (probe-fed hemispherical DRA). To evaluate the robustness of multirate schemes on a practical EM problem, we use an example of the coaxial probe-fed hemispherical DRA experiment from [6]. That work contained a comparison of a second-order finite volume time domain scheme against a simulation using the commercial software HFSS for a large dielectric hemisphere antenna with small feed coaxial cable. The DRA including all required geometrical parameters is presented in Figure 5. The outer boundary of the computational domain is an ellipsoid with absorbing boundary conditions from (1). Computational results are compared with the ones presented in [6] for the same set of parameters. As in [6] an S_{11} parameter of the antenna is computed. Baumann [6] used the entire port section for the original way of reflection coefficient computations. Because of the third-order accuracy we are able to compute the return loss from a single observation point. To do that as in [6] we impose an analytic field onto the coaxial cable entrance port with wide-enough Gaussian (56) to cover the desirable frequency domain. Then we register the field $E_z^{\text{point}}(t)$ at one observation point with coordinates $(0.00144, 0.0065, -0.00475)$, and compute the analytic field $E_z^{\text{coax}}(t)$ in the coaxial cable in the same point. Then the reflected coefficient is computed at several frequency points using

$$S_{11}(F) = 20\log_{10}\frac{|f\,E_z^{\text{coax}}(F) - f\,E_z^{\text{point}}(F)|}{|f\,E_z^{\text{coax}}(F)|}\,[\text{dB}], \qquad (59)$$

where $f\,E_z(F) = \int_0^T E_z(t)\exp(-2\pi i F t)\,dt$ is computed for a set of frequencies $3\,\text{GHz} \le F \le 6\,\text{GHz}$. Our third-order single point result is closer to the curve
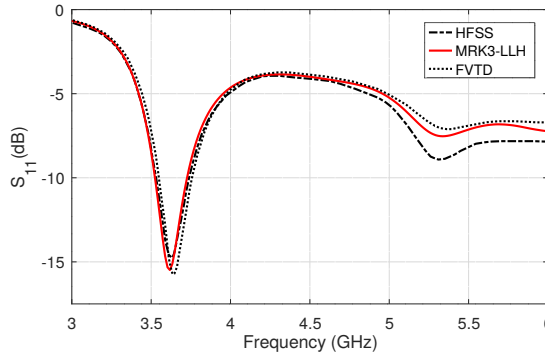
Figure 6. Return loss DRA S_{11} coefficient.

scheme	# of Δt_g	$n(LU)$	$\frac{n(LU)_{RK3}}{n(LU)}$	CPU [s]	$\frac{CPU_{RK3}}{CPU}$	$\frac{\|S_{11} - S_{11}^{RK3}\|_2}{\|S_{11}^{RK3}\|_2}$
RK3	170 847	97 792 310 259	1	65 301	1	0
MRK3-TW-P2	2 670	26 009 562 030	3.76	18 965	3.44	1.48×10^{-2}
MRK3-TW-OP	1 810	24 000 306 780	4.07	18 551	3.52	2.01×10^{-2}
MRK3-LLH-P2	2 670	24 471 455 130	4.00	17 150	3.8	1.29×10^{-5}
MRK3-LLH-OP	2 171	21 515 239 590	4.55	16 834	3.88	1.97×10^{-5}

Table 8. DRA: performance of MRK3 schemes compared to single-rate RK3, where $n(LU)$ is the number of flux operations. The last column shows the relative difference of S_{11}^{RK3} computed with Runge–Kutta to S_{11} obtained from MRK3 schemes.

obtained with HFSS (Figure 6). Higher-order schemes conduct more high-frequency oscillations, which is visible for higher than 5 GHz reflections. Performance evaluation of our implementation is shown in Table 8. The simulation speedup achieved in our experiments using a third-order scheme is similar to the one reported in [15] for the same problem but using a different mesh and second-order scheme.

6. Summary

In this paper two multirate schemes with SSP RK3 base method are tested in application to Maxwell's equations on unstructured tetrahedral meshes. The order conditions for MPRK schemes on linear problems show that the third-order extension of the scheme proposed in [38] has only first-order accurate coupling, while the scheme developed in [27] is third-order accurate for linear problems with three-stage third-order Runge–Kutta methods. For 3D simulations, both schemes are flexible in terms of local time-step partition allowing higher speedup than previously reported in the literature even for more expensive third-order approximation. Solution error comparisons confirm that the analysis based on order conditions is valid in 3D

simulations. Moreover, our numerical results show that arbitrary time-step ratio does not compromise the accuracy of simulations. Future work may include extending the implementation of multirate schemes to higher order for 3D simulations.

Acknowledgments

References

[1] P. Albrecht, *The Runge–Kutta theory in a nutshell*, SIAM J. Numer. Anal. **33** (1996), no. 5, 1712–1735. MR Zbl

[2] J. F. Andrus, *Numerical solution of systems of ordinary differential equations separated into subsystems*, SIAM J. Numer. Anal. **16** (1979), no. 4, 605–611. MR Zbl

[3] ———, *Stability of a multi-rate method for numerical integration of ODEs*, Comput. Math. Appl. **25** (1993), no. 2, 3–14. MR Zbl

[4] L. D. Angulo, J. Alvarez, F. L. Teixeira, M. F. Pantoja, and S. G. Garcia, *Causal-path local time-stepping in the discontinuous Galerkin method for Maxwell's equations*, J. Comput. Phys. **256** (2014), 678–695. MR Zbl

[5] C. A. Balanis, *Advanced engineering electromagnetics*, Wiley, 1989.

[6] D. Baumann, *A 3-d numerical field solver based on the finite-volume time-domain method*, Ph.D. thesis, ETH Zürich, 2006.

[7] P. Bonnet, X. Ferrieres, F. Issac, F. Paladian, J. Grando, J. C. Alliot, and J. Fontaine, *Numerical modeling of scattering problems using a time domain finite volume method*, J. Electromagnet. Wave. **11** (1997), no. 8, 1165–1189.

[8] F. Collino, T. Fouquet, and P. Joly, *A conservative space-time mesh refinement method for the 1-D wave equation, I: Construction*, Numer. Math. **95** (2003), no. 2, 197–221. MR Zbl

[9] ———, *Conservative space-time mesh refinement methods for the FDTD solution of Maxwell's equations*, J. Comput. Phys. **211** (2006), no. 1, 9–35. MR Zbl

[10] E. M. Constantinescu and A. Sandu, *Multirate timestepping methods for hyperbolic conservation laws*, J. Sci. Comput. **33** (2007), no. 3, 239–278. MR Zbl

[11] C. Dawson and R. Kirby, *High resolution schemes for conservation laws with locally varying time steps*, SIAM J. Sci. Comput. **22** (2000), no. 6, 2256–2281. MR Zbl

[12] S. Descombes, S. Lanteri, and L. Moya, *Locally implicit time integration strategies in a discontinuous Galerkin method for Maxwell's equations*, J. Sci. Comput. **56** (2013), no. 1, 190–218. MR Zbl

[13] J. Diaz and M. J. Grote, *Energy conserving explicit local time stepping for second-order wave equations*, SIAM J. Sci. Comput. **31** (2009), no. 3, 1985–2014. MR Zbl

[14] A. Ezziani and P. Joly, *Local time stepping and discontinuous Galerkin methods for symmetric first order hyperbolic systems*, J. Comput. Appl. Math. **234** (2010), no. 6, 1886–1895. MR Zbl

[15] C. Fumeaux, D. Baumann, P. Leuchtmann, and R. Vahldieck, *A generalized local time-step scheme for efficient FVTD simulations in strongly inhomogeneous meshes*, IEEE T. Microw. Theory **52** (2004), no. 3, 1067–1076.

[16] C. W. Gear and D. R. Wells, *Multirate linear multistep methods*, BIT **24** (1984), no. 4, 484–502. MR Zbl

[17] N. Goedel, S. Schomann, T. Warburton, and M. Clemens, *Local timestepping discontinuous Galerkin methods for electromagnetic RF field problems*, 3rd European Conference on Antennas and Propagation, IEEE, 2009, pp. 2149–2153.

[18] M. J. Grote and T. Mitkova, *Explicit local time-stepping methods for Maxwell's equations*, J. Comput. Appl. Math. **234** (2010), no. 12, 3283–3302. MR Zbl

[19] _____ , *High-order explicit local time-stepping methods for damped wave equations*, J. Comput. Appl. Math. **239** (2013), 270–289. MR Zbl

[20] M. Günther, A. Kværnø, and P. Rentrop, *Multirate partitioned Runge–Kutta methods*, BIT **41** (2001), no. 3, 504–514. MR Zbl

[21] E. Hairer, *Order conditions for numerical methods for partitioned ordinary differential equations*, Numer. Math. **36** (1981), no. 4, 431–445. MR Zbl

[22] R. F. Harrington, *Time-harmonic electromagnetic fields*, McGraw-Hill, 1961.

[23] W. Hundsdorfer, A. Mozartova, and V. Savcenco, *Monotonicity conditions for multirate and partitioned explicit Runge–Kutta schemes*, Recent developments in the numerics of nonlinear hyperbolic conservation laws (R. Ansorge, H. Bijl, A. Meister, and T. Sonar, eds.), Notes Numer. Fluid Mech. Multidiscip. Des., no. 120, Springer, 2013, pp. 177–195. MR Zbl

[24] Z. a. Jackiewicz and R. Vermiglio, *Order conditions for partitioned Runge–Kutta methods*, Appl. Math. **45** (2000), no. 4, 301–316. MR Zbl

[25] G.-S. Jiang and C.-W. Shu, *Efficient implementation of weighted ENO schemes*, J. Comput. Phys. **126** (1996), no. 1, 202–228. MR Zbl

[26] M. Kotovshchikova, D. K. Firsov, and S. H. Lui, *A third order finite volume WENO scheme for Maxwell's equations on tetrahedral meshes*, Commun. Appl. Math. Comput. Sci. **13** (2018), no. 1, 87–106. MR Zbl

[27] L. Liu, X. Li, and F. Q. Hu, *Nonuniform time-step Runge–Kutta discontinuous Galerkin method for computational aeroacoustics*, J. Comput. Phys. **229** (2010), no. 19, 6874–6897. MR Zbl

[28] N. Manzanares-Filho, C. A. A. Moino, and A. B. Jorge, *An improved controlled random search algorithm for inverse airfoil cascade design*, 6th World Congress on Structural and Multidisciplinary Optimization (J. Herskovits, S. Mazorche, and A. Canelas, eds.), COPPE, 2005.

[29] E. Montseny, S. Pernet, X. Ferriéres, and G. Cohen, *Dissipative terms and local time-stepping improvements in a spatial high order discontinuous Galerkin scheme for the time-domain Maxwell's equations*, J. Comput. Phys. **227** (2008), no. 14, 6795–6820. MR Zbl

[30] S. Osher and R. Sanders, *Numerical approximations to nonlinear conservation laws with locally varying time and space grids*, Math. Comp. **41** (1983), no. 164, 321–336. MR Zbl

[31] S. Piperno, *Symplectic local time-stepping in non-dissipative DGTD methods applied to wave propagation problems*, M2AN Math. Model. Numer. Anal. **40** (2006), no. 5, 815–841. MR Zbl

[32] J. R. Rice, *Split Runge–Kutta method for simultaneous equations*, J. Res. Nat. Bur. Standards **64B** (1960), 151–170. MR Zbl

[33] A. Sandu and E. M. Constantinescu, *Multirate explicit Adams methods for time integration of conservation laws*, J. Sci. Comput. **38** (2009), no. 2, 229–249. MR Zbl

[34] M. Schlegel, O. Knoth, M. Arnold, and R. Wolke, *Multirate Runge–Kutta schemes for advection equations*, J. Comput. Appl. Math. **226** (2009), no. 2, 345–357. MR Zbl

[35] B. Seny, J. Lambrechts, R. Comblen, V. Legat, and J.-F. Remacle, *Multirate time stepping for accelerating explicit discontinuous Galerkin computations with application to geophysical flows*, Internat. J. Numer. Methods Fluids **71** (2013), no. 1, 41–64. MR Zbl

[36] G. R. Shubin and J. B. Bell, *A modified equation approach to constructing fourth-order methods for acoustic wave propagation*, SIAM J. Sci. Statist. Comput. **8** (1987), no. 2, 135–151. MR Zbl

[37] J. L. Steger and R. F. Warming, *Flux vector splitting of the inviscid gasdynamic equations with application to finite-difference methods*, J. Comput. Phys. **40** (1981), no. 2, 263–293. MR Zbl

[38] H.-z. Tang and G. Warnecke, *High resolution schemes for conservation laws and convection-diffusion equations with varying time and space grids*, J. Comput. Math. **24** (2006), no. 2, 121–140. MR Zbl

[39] A. Taube, M. Dumbser, C.-D. Munz, and R. Schneider, *A high-order discontinuous Galerkin method with time-accurate local time stepping for the Maxwell equations*, Int. J. Numer. Model. El. **22** (2009), no. 1, 77–103. Zbl

[40] Y.-T. Zhang and C.-W. Shu, *Third order WENO scheme on three dimensional tetrahedral meshes*, Commun. Comput. Phys. **5** (2009), no. 2–4, 836–848. MR Zbl

MARINA KOTOVSHCHIKOVA: `m.a.kotovshchikova@gmail.com`
San Jose, CA United States

DMITRY K. FIRSOV: `d.k.firsov@gmail.com`
San Jose, CA, United States

SHIU HONG LUI: `luish@cc.umanitoba.ca`
Department of Mathematics, University of Manitoba, Winnipeg, MB, Canada